Chapter II

Synthesis, characterization, and laser-irradiated analysis of semiconducting nanostructured TMDC systems

"Knowledge is the eye of desire and can become the pilot of the soul"

- Will Durant

2.1 Introduction

Nanosheets (single-layer, few-layer/multi-layer), inorganic fullerene (IF)-like structures, and nanotubes are some of the most widely investigated forms of layered transition metal dichalcogenides (TMDCs). In 1904, Hintze reported that some TMDC materials have complete basal cleavage properties. Accordingly, in 1923, Linus Pauling gave an account of the cleaving of MoS_2 crystal down to a thickness of 0.23 mm [2]. In 1963, R. Frindt reported MoS_2 of thickness as low as 50 nm [3]. In 1966, approximately 3.5-4 nm thick nanosheets were obtained [4]. Finally, single-layer MoS_2 and WS_2 were synthesized in 1986 [5] and in 1988 [6] respectively. In the beginning years of the development of single-layer TMDCs, the synthesis of WS_2 and MoS_2 single layers was performed using the lithium intercalation method. As described in *chapter I*, several exfoliation methods have been explored over time. One of such methods is liquid-mediated exfoliation. In this method, bulk flakes of TMDCs (size ~µm) are placed in a suitable solvent and the mixture is subjected to sonication. It is then followed by centrifugation to obtain nanostructures of TMDCs. This method is also known as solvo-sonication. After a thorough investigation of liquid-mediated exfoliation, Coleman *et al.* [7] proclaimed that N-methyl-2-pyrrolidone (NMP) and isopropanol (IPA) were the finest solvents for the exfoliation of TMDCs. The simplicity, scalability, and consistency of the solvo-sonication method motivate us to use it throughout this thesis. Besides, we also took this advantage of using the same solvent to exfoliate both WS_2 and MoS_2.

Fullerene is a closed form of graphite, where carbon atoms form closed ring cage-like structure. The structural analogy between graphite and TMDC compounds suggest that closed structures may also exist in TMDCs materials. Tenne *et al.* turned this possibility into reality by initially synthesizing IFs and nanotubes of WS_2 [8]. This ground-breaking discovery was followed by synthesis of IFs of MoS_2 [9], WSe_2, and $MoSe_2$ [10]. WS_2 IF were obtained by annealing WS_2 films on quartz substrate at 1000°C in H_2S [8], while MoS_2 IF were obtained by first oxidizing the MoS_2 films, then firing them at 850-1050°C in a steam of H_2S and N_2/H_2 mixture [9]. Later different other routes [11] and hydrothermal processes [12] were applied to synthesize such types of nanostructures.

Lasers with different excitation wavelengths were also employed to synthesize IFs [13-17]. It has been observed that laser-irradiated techniques are easy to perform, material-independent and important for location-specific treatments [15]. Such novelties in the laser-irradiation technique inspired us to carry out laser-irradiated analysis on the WS_2 nanosheet system which will be discussed in the coming sections.

2.2 WS_2 and MoS_2 nanosheets

Layered TMDC materials exhibit complete basal cleavage; therefore, it is possible to exfoliate these materials down to a single-layer thickness of 7-10 Å [18]. After exfoliation of these materials, flat, plate-like nanostructures are obtained. If the thicknesses of these nanostructures are in the range of 1-100 nm, then these nanostructures are termed as nanosheets. A single-layer nanosheet is called a monolayer. However, there is no exact definition for a few layers or multiple layers. Most researchers use the term few layers to interpret number of layers less than 10 [19-24] However, some consider up to 74 layers to be few-layer [25]. Sometimes, the terms few-layer and multilayer are used interchangeably [26].

In this thesis work, we will consider a nanosheets to be few layered when the number of layers in the structure ≤ 15, while all the nanosheets above this limit will be considered as multilayered.

2.2.1 Liquid-mediated exfoliation of WS_2 and MoS_2

For the direct exfoliation method, bulk WS_2 flakes were purchased from Sigma-Aldrich, Product No. 24369-50G. MoS_2 bulk was purchased from Loba Chemie (Assay min 98%, Product code:0469500100). The size of the bulk flakes was of ~2 µm, and the assay min was 99.9%. N-methyl Pyrrolidone (NMP, assay min > 99.5%) was purchased from

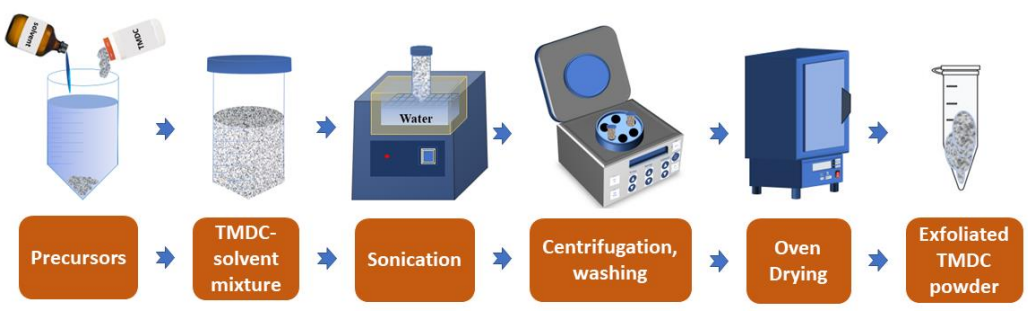

Fig.2.1. Preparation steps involved in the synthesis of TMDC nanosheets through liquid-mediated exfoliation.

Merck®. Bulk TMDCs were separately mixed with NMP at a concentration of 1.5 mg mL^{-1}. The WS_2-NMP and MoS_2-NMP mixtures were ultrasonicated for ~ 4 h in an ultrasonic bath sonicator, UD100SH-2.8LQ, with an output power of 100 W. During sonication, the temperature of the liquid medium (water) was maintained below 30 °C. The mixtures were shaken in every 10 min for the initial one hour. Then they were shaken after every half hour for the remaining period. This was performed to avoid precipitation of the TMDC flakes at the bottom of the container. Afterwards, the exfoliated mixture was centrifuged for 15 min at 3000 rpm in Remi Centrifuge. The obtained pellets of TMDCs were washed several times with double distilled (DD) water and dried for approximately 12 h at 60-65 °C. This was then kept for characterization. The steps involved in the preparation process is illustrated in **Fig 2.1**.

Analysis of structural, vibrational, and optical properties of the as-prepared nanosheets are given below.

2.2.2 Crystallographic analysis

The conventional method for structural characterization of polycrystalline materials is powder X-ray diffraction spectroscopy (p-XRD). An X-ray diffraction spectrometer (BRUKER AXS, Germany) was employed for the structural analysis of the synthesized nanosheets throughout the thesis. It utilizes a CuKα line (λ=1.54 Å) as the X-ray source. The X-ray diffraction spectra of bulk and exfoliated systems of WS_2 and MoS_2 are shown in **Fig 2.2 (a)** and **(b)**. It was observed that the bulk and exfoliated WS_2 and MoS_2 follow the standard X-ray diffraction pattern of JCPDS No. 84-1398 and JCPDS No. 37-1492 respectively. This confirms that, hexagonal crystallographic phase is dominant, having space group $P6_3$ mmc and space group number 194. In WS_2 systems, it is observed that diffraction peaks are positioned around 2θ=14.3°, 28.8°, 32.7°, 33.4°, 34.9°, 39.4°, 43.9°, 49.5°, 58.3° and 59.8° corresponding to crystallographic plane (002), (004), (100), (101), (102), (103), (006), (105), (110) and (008) respectively. In case of MoS_2 system, diffraction peaks 14.3°, 29.01°, 32.7°, 33.5°, 35.8°, 39.5°, 44.1°, 49.8°, 56.0°, 58.3° and 59.9° may be assigned for (002), (004), (100), (101), (102), (103), (006), (105), (106), (110) and (008) planes respectively.

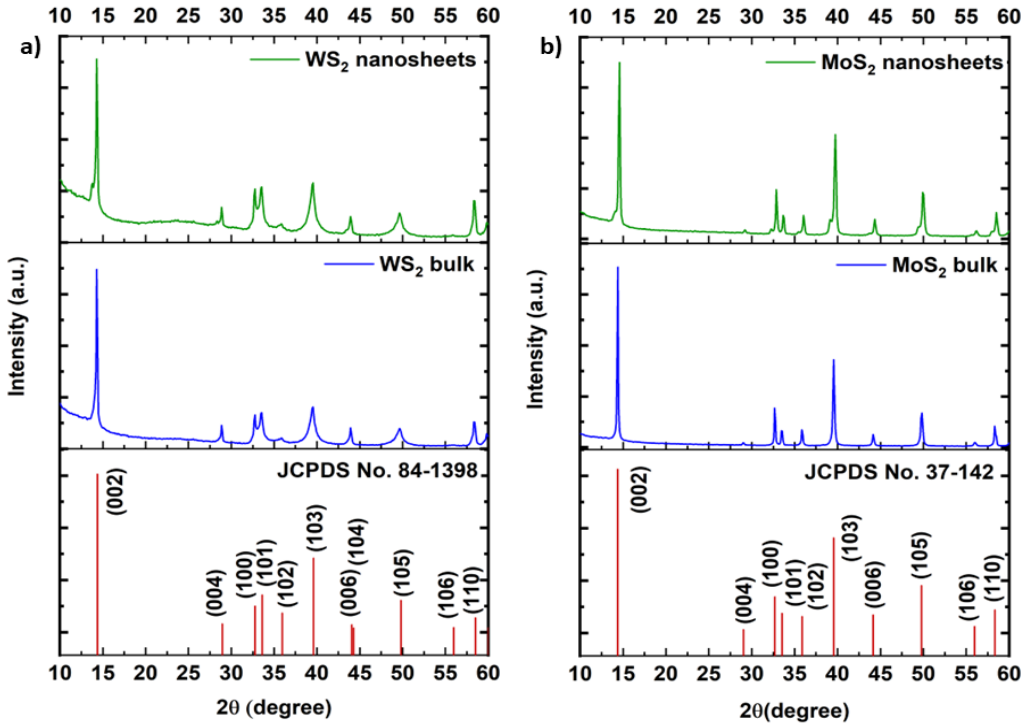

Fig.2.2. X-ray diffraction spectra of **(a)** WS_2 bulk and nanosheets **(b)** MoS_2 bulk and nanosheets.

2.2.3 Morphological analysis of WS_2 and MoS_2 nanosheets

Field Emission Scanning electron microscopy (FESEM) is a common technique to study the morphological characteristics of nanostructures. FESEM micrographs of WS_2 and MoS_2 nanosheets are shown in **Fig 2.3 (a)** and **Fig 2.3 (b)** respectively. Both the images confirm the hexagonal structure of the exfoliated systems and inhomogeneous exfoliation of WS_2 and MoS_2 nanosheets. They have multi-layered structures.

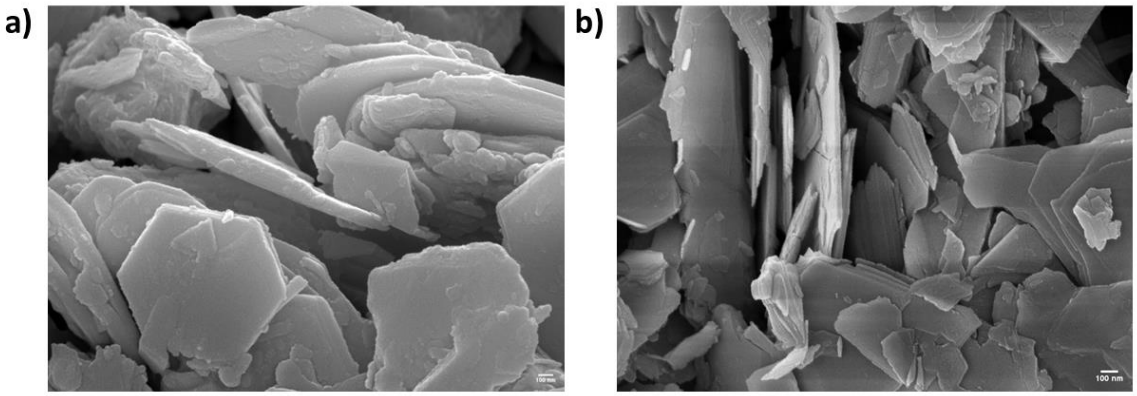

Fig.2.3. FESEM micrographs of (**a)** WS_2 and (**b)** MoS_2 nanosheets.

2.2.4 Raman Spectroscopic data analysis of WS_2 and MoS_2 nanosheets

Raman spectroscopy is a non-invasive (when operated in a controlled manner) technique to study the vibrational characteristics of the Raman active materials. It has been observed that Raman spectroscopy can also be used to determine the number of layers in a layered material. Here, Raman spectrometer by Ranishaw®, associated with 514.5 nm green laser source was used to obtain the Raman data for all the samples throughout the thesis. The Raman spectra for the material specimen are presented in **Fig 2.4**. In the Raman spectroscopic data, multi-peak Lorentzian fitting was applied for both bulk and nanostructure systems. This is a convenient way to separate overlapping modes. In case of WS_2, Raman active modes *LA, (2LA -2E$^2_{2g}$), 2LA, 2LA-2E$^2_{2g}$, E$^1_{2g}$, A$_{1g}$, (A$_{1g}$+LA)* and 4*LA* are located at 173 cm^{-1}, 295 cm^{-1}, 349 cm^{-1}, 354 cm^{-1}, 419 cm^{-1}, 582 cm^{-1} and 696 cm^{-1}. Similarly, for MoS_2, peaks are located at 284 cm^{-1}, 380 cm^{-1}, 406 cm^{-1}, 451 cm^{-1}, 759 cm^{-1} which correspond to *E$_{1g}$, E$^1_{2g}$, A$_{1g}$, 2LA* and respectively *2E$^1_{2g}$* [27-29]. There are different parameters which ensure the exfoliation of the bulk systems e.g., *E/A* ratio. In bulk WS_2, *E/A* ratio is ~ 0.14 and for exfoliated WS_2 it is ~0.52. Similarly, in bulk MoS_2 *E/A* ratio is ~ 0.48 and for exfoliated MoS_2, it is ~0.52. The increase in *E/A* ratio with exfoliation ensures the exfoliation [30].

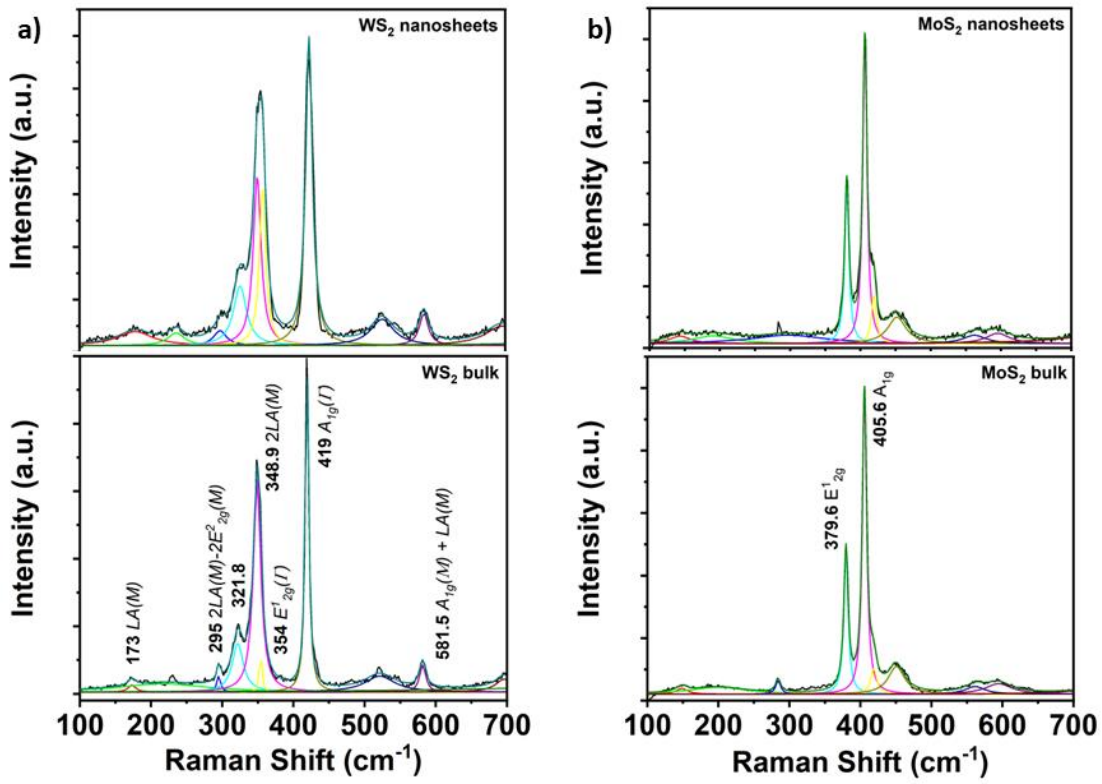

Fig.2.4 Raman Spectra of bulk and nanosheets of (**a)** WS_2 and (**b)** MoS_2.

2.2.5 UV-vis spectroscopic data analysis of WS_2 and MoS_2 nanosheets

UV-vis spectroscopic analysis provides an insight into the electronic band structure of the material and it helps to confirm many fundamental interactions. In the first report on absorption spectra of single crystal MoS_2, Frindt *et al.* [3] suggested that the sharp absorption peaks A and B occur due to formation of exciton states, so as the peak C. Peaks A and B arise because of direct gap transition at the *K* point from split valence bands. The splitting is due to the spin-orbit interaction. Likewise, other higher energy peak (C) may arise due to transition from other values of the wave-vector or deeper valence bands to the conduction band [3, 31,32]. These explanations are also applicable to WS_2 nanosheets. **Fig 2.5** clearly shows absorption spectra of both WS_2 and MoS_2 nanosheets in the visible region. In the UV-vis spectra of WS_2 (**Fig. 2.5 (a)**), sharp absorption peak at ~ 636 nm (A), shoulder peaks at ~ 530 nm (B) and ~ 462 nm (C) have been observed. Peaks A and B arise because of direct gap transition at the *K* point [26,33, 34]. Similarly, peak C corresponds to optical transition between the densities of states peaks in the valence band and conduction band [35]. **Fig. 2.5 (b)** shows sharp absorption peak of MoS_2 at ~ 672 nm (A), shoulder peaks at ~ 610 nm (B) and ~ 448 nm (C).

Based on these properties of the as-prepared nanostructures, in the later sections, synthesis steps were optimized according to the requirement of the investigation.

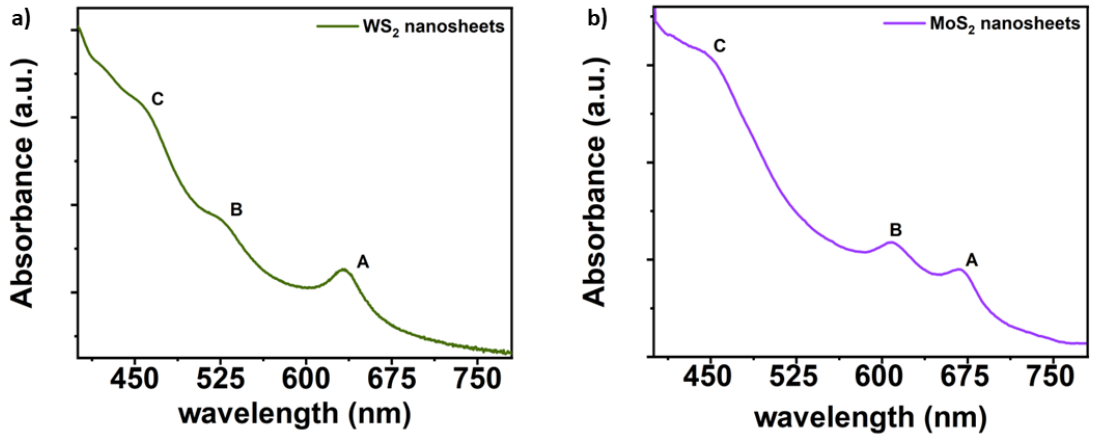

Fig.2.5. Absorption spectra of (**a)** WS_2 and (**b)** MoS_2 nanosheets.

2.3 Laser assisted phase transition and formation of inorganic fullerene (IF)-like WS_2 nanostructures

It was already mentioned in c*hapter I* that TMDCs are usually found in polymorphs such as *1T, 2H, 3R* and *1T'*. Polymorphs differ by their symmetries and structures. Eventually, different polymorphs are likely to exhibit different material properties [36–39]. Several reports have confirmed that *1T* phase outperforms *2H* phase in catalytic activity and conductivity, while the *2H* phase outperforms *1T* in photo-absorption and emission [40-42]. Due to such polymorph-based properties, there are persistent efforts to trigger phase transitions in these materials. Phase transitions in layered materials can be initiated by different methods such as intercalation [40, 43, 44], pressure [45], strain [46] etc. Voiry *et al.* prepared a *1T* phase-dominated layered system, using an intercalation technique with enhanced functionalities such as enhanced catalytic property, conductivity etc. [40]. The application of pressure (~ GPa) is a novel method for initiating phase transition from *1H* to *1T′* in WS_2 systems [45]. Kasmola *et al.* introduced tensile strain on WS_2 flakes by performing thermal annealing of a WS_2/Au/mica system, inducing a *2H-1T* phase transition [46]. Electrochemical synthesis is another technique for inducing a phase transition from *2H* to *1T* [41]. In addition, light- and laser-driven techniques introduce a phase transition from *1T* to *1H* in a CVD-grown WS_2 system following the *Johnson (Mehl–Avrami) Kolmogorov* model [47]. Although laser-assisted techniques are rare compared to intercalation [40, 48, 49] and doping [50] techniques for *H-T* transition, laser-driven techniques are robust because of their usefulness in the non-contact mode and for generation of local effects. For-instance, a laser-induced heterophase homojunction contact can bridge hexagonal (*2H*) and monoclinic (*1T'*) $MoTe_2$ with a lower contact potential [51]. Recently, different laser-assisted phase change techniques have been developed for different layered materials [47,52-54]. However, the phase transition from *2H* to *1T* is rare. If we further investigate the benefits of using a laser, we will observe that the use of a laser can locally oxidize the material, thereby changing its properties locally [55]. The introduction of oxygen into the system enhances its conductivity [56]. Moreover, laser irradiation can be considered as another method for heating. As such, it is likely to affect the exfoliation of the system. Apparently, laser-induced exfoliation has been observed in many laser-induced processes [51,53,57]. Along with the evolution of new phonon modes, laser-induced phonon shifts are common in laser-assisted processes [58,59].

From the above discussion, it is evident that laser irradiation can substantially impact TMDC properties. Therefore, it is necessary to have considerable knowledge of the impact of laser irradiation on TMDC material before using them in laser-based applications. Besides, laser-induced nanostructures are gaining attention due to their multidimensional sensing properties [60]. Being, inspired by laser-induced phenomena in TMDC materials, laser-irradiated investigation was performed on nanostructured WS_2 system. Accordingly, the remaining sections of this chapter are dedicated to synthesis of WS_2 nanosheets and effect of laser irradiation on it.

2.3.1 Exfoliation of WS_2

WS_2 flakes, purchased from Sisco Research laboratories (SRL), assay min 99.9%, were mixed with NMP at a concentration of 1.6 mg ml^{-1}. The mixture was then ultrasonicated (for 3 h) at temperatures below 30°C and left undisturbed for 24 h. The supernatant was a homogeneous yellowish dispersion of WS_2 with greyish pallets at the bottom. This system was then centrifuged at 25 °C with 1500 RCF (relative centrifugal force) for 45 min using a 5430 R centrifuge (Eppendorf). After centrifugation, top 2/3rd of the WS_2-solvent was gently pipetted out from the rest of the solution, and characterizations were performed. The remainder of the sample was washed with ethanol. The drying process was performed at 60 °C in a hot air oven. The final product was stored in an airtight vial for further

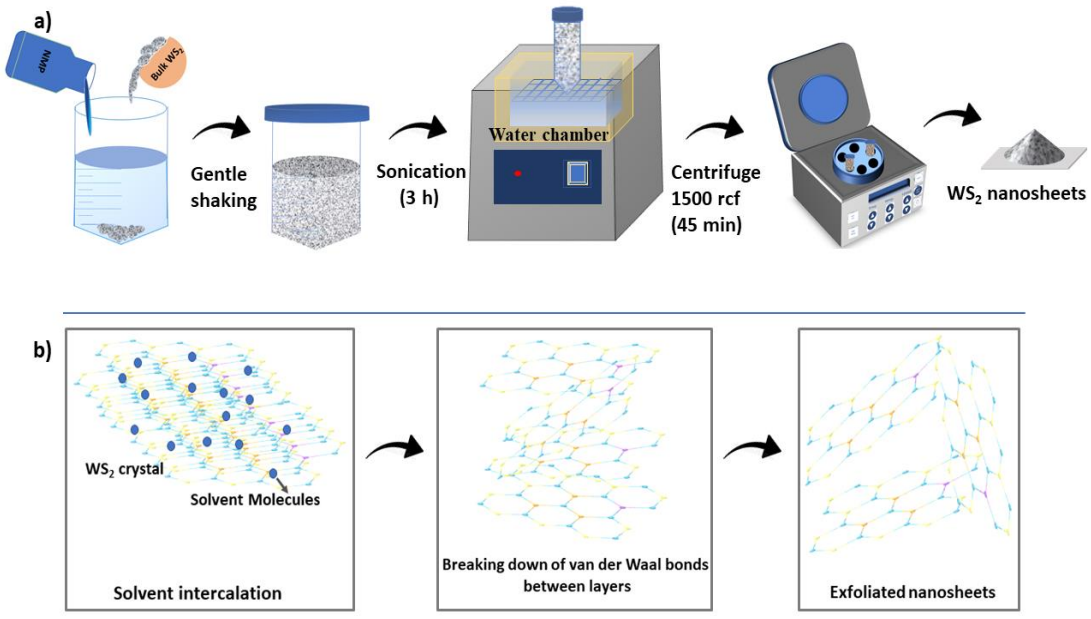

Fig.2.6. Preparation steps of WS_2 nanostructures and associated changes in the bulk WS_2 over different physiochemical treatments.

characterization. The preparation steps of WS_2 nanostructures and associated changes in the material system are shown in **Fig. 2.6.**

2.3.2 Instrumentation

TEM micrographs of the exfoliated WS_2 were acquired using a Transmission Electron Microscope (TEM by FEI COMPANY, USA). SEM images of the exfoliated WS_2 flakes were collected using JOEL FESEM. For the Raman characterization, a Raman spectroscope equipped with an Ar^+ laser line (λ_{exc} = 514 nm) by RENISHAW was used. During the investigation, laser powers of 0.025, 0.05, 0.25, 0.5, 2.5, and 5 mW were applied. X-ray diffraction spectroscopy was performed using an X-ray diffractometer (BRUKER AXS, GERMAN). The absorption characteristics of the exfoliated samples were recorded in the wavelength range of 200-800 nm using a UV-vis spectrophotometer (SHIMADZU-2450).

2.3.3 Results and discussions

Fig. 2.7(a) is the photograph of the homogeneously dispersed exfoliated WS_2 in NMP, which are stable over several days. **Fig. 2.7(b)** shows the absorption spectra of the dispersion. Excitonic absorption peaks A, B, and C were observed at around 631.45 nm (~1.96 eV), 527.9 nm (~2.35 eV), and 459.4 nm (~2.7 eV) [61, 62] where A and B correspond to direct band gap transition [33,34,63]. The energy difference between A and B excitonic peaks are generally attributed to the measure of strength of spin-orbit coupling [64]. Peak C corresponds to optical transition between the 'densities of states' peaks in the valence band and conduction band [35] as discussed in earlier sections. **Fig. 2.7(c)** shows a field-emission SEM micrograph of the exfoliated WS_2, confirming the hexagonal structure of the exfoliated samples. An enlarged view of one of the exfoliated sheets is presented in the inset. The average flake thickness was found to be 106 nm after multiple flake measurements (**AT1[#]**), which implies the multilayer nature of the exfoliated WS_2 specimens. **Fig.2.8 (a)** shows the Raman spectra of laser-irradiated WS_2 nanosheets. 514 nm green laser with different powers, viz. 0.025 mW, 0.05 mW, 0.25 mW, 0.5 mW, 2.5 mW and 5 mW were employed for this. The exposure time was 10 s for all measurements. With increase in laser power, the signal-to-noise ratio increases, which is further accompanied by intensity enhancement as well as the evolution of the majority of the vibrational modes (**AT2[$]**). It is clearly observed that with an increase in laser power, the

[#, $] **Appendix**

prominent phonon modes E^1_{2g} and A_{1g} of *2H*-WS_2 eventually become red-shifted(**A1**[€]). All the graphs, except the one in black, show Raman spectra of a typical *2H*-WS_2 [27].

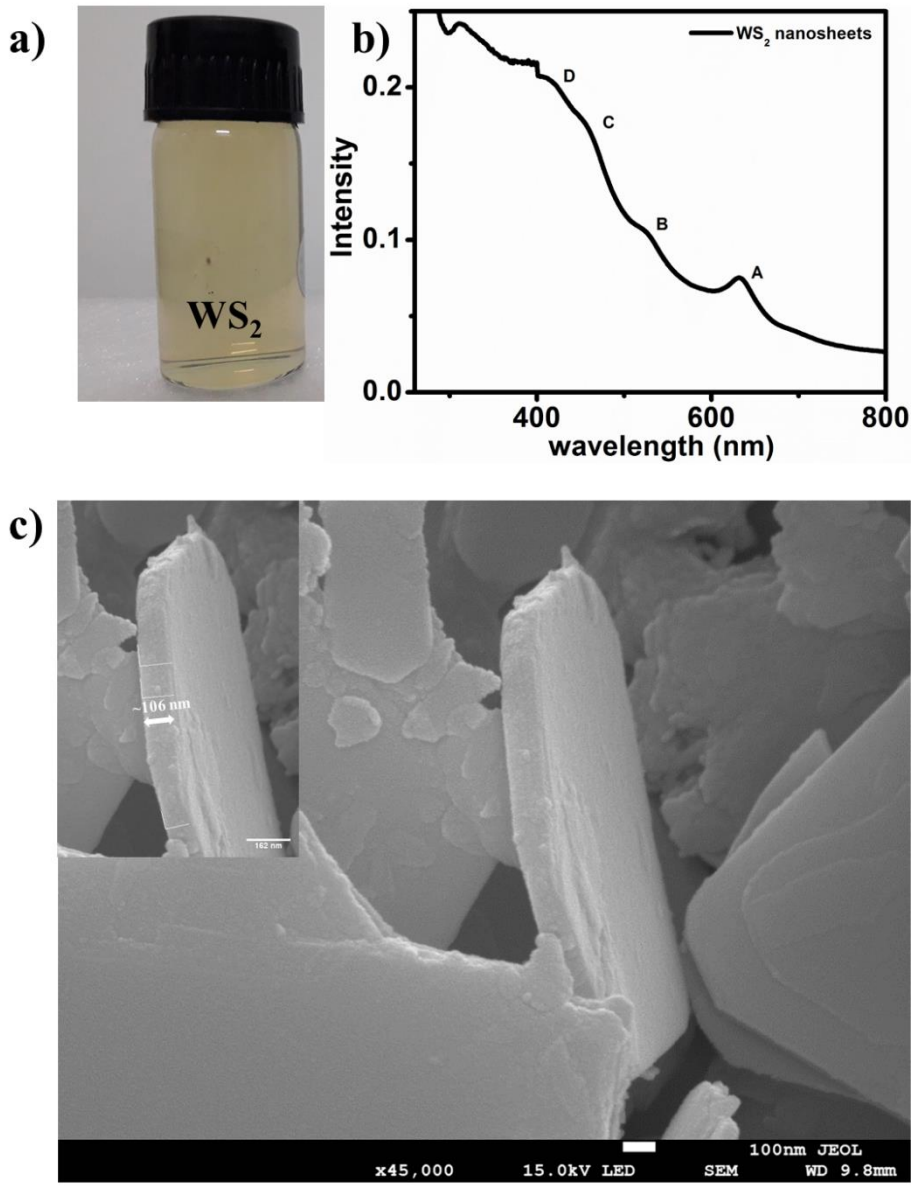

Fig.2.7. (a) Photograph of WS_2 nanostructures dispersed in NMP **(b)** absorption spectra of the dispersed nanosheets **(c)** SEM micrograph of WS_2 nanosheets.

As the power was increased from 2.5 mW to 5 mW, a few new vibrational modes appeared in the spectra, as represented by P, Q, R, S, T, and U. These new modes cannot be directly attributed to un-treated *2H*-WS_2. To investigate the origin of the newly evolved peaks, Raman spectral analysis was performed for different laser exposure times (different laser energies). The exposure time-dependent analysis (**Fig. 2.8(b))** shows that the relative intensities of *E* and *A* modes decreases with increasing exposure time, suggesting the

[€]**Appendix**

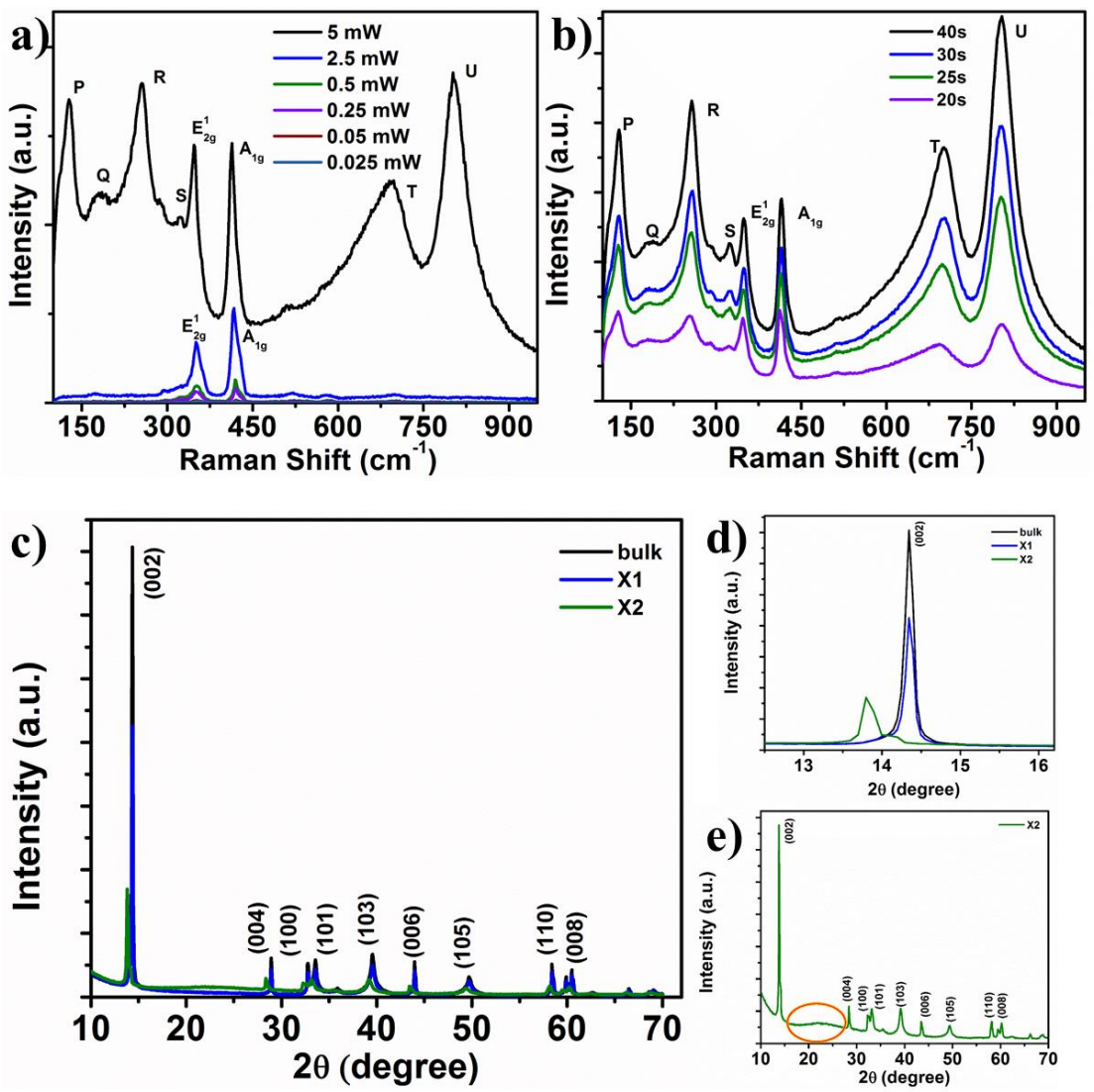

Fig.2.8. Raman spectra of WS_2 nanostructures irradiated with laser (514 nm green) having different **(a)** laser powers (0.025, 0.05, 0.25, 0.5, 2.5 and 5mW) and **(b)** exposure time (10, 25, 30 and 40 s); **(c)** XRD spectra of bulk, untreated (X1) and laser treated (X2) WS_2 nanosheets **(d)** diffraction peak corresponding to (002) plane for X2, X1 and bulk. A clear shift in diffraction angle is observed for X2, compared to bulk and X1, **(e)** XRD spectra of X2. A weak diffraction peak is observed in the highlighted region (between 20°–30°). This is attributed to the diffraction peak of oxidized WS_2 nanosheets.

weakening of the *2H*-WS_2 phase, while the newly evolved T and U peaks increase with increasing exposure time. Interestingly, in contrast to T and U, the newly evolved P, R, and S peaks decreased over time (**A2, A3**$^{\Psi}$). This observation indicates that the lower and higher energy peaks are neither directly related nor of the same origin. The higher energy peaks U and T (around 805 cm^{-1} and 698 cm^{-1}, for laser power 5 mW, exposure time 40 s) may correspond to the O-W-O stretching mode, as previously reported [65–68]. On the other hand, the lower energy peaks (129 cm^{-1}, 257 cm^{-1}, 189 cm^{-1}, for laser power of 5

$^{\Psi}$**Appendix**

mW, exposure time of 40 s correspond to *1T* WS_2, as previously reported [21,40,69]. Moreover, a peak within 514 nm and 517.5 nm were observed as the exposure time increased. According to Berkdemir *et al.* [27], this is a resonant peak occurring owing to the excitation of the sample with a 514 nm laser. The XRD spectra of bulk WS_2, WS_2 nanosheets, and laser-treated nanosheets are shown in **Fig. 2.8(c).** X1 represents the XRD spectra of the untreated WS_2 nanosheets and X2 represents the laser (5 mW)-treated WS_2 nanosheets. The bulk and untreated WS_2 nanosheets (bulk, X1) exhibit prominent diffraction peaks around 14.34º, 28.91º, 32.78 º, 33.55 º, 35.68 º, 39.55 º, 43.98 º, 49.71 º, 58.42 º, 59.89 º and 60.49 º**,** which correspond to the (002), (004), (100), (101), (102), (103), (006), (105), (110), (008) and (112) crystal planes (JCPDS no. 84–1398). However, for the treated sample X2, a clear splitting and shift of the diffraction peaks towards smaller angles were observed. The shift in the diffraction peak corresponding to the (002) plane is shown in **Fig. 2.8(d)**. The shifting and evolution of the peaks due to laser irradiation on the sample indicates initiation of a new phase in the system [69]. Moreover, a decrease in the intensity of the diffraction peaks corresponding to the (002) plane can be observed in **Fig. 2.8(c**). The diffraction peak intensity corresponding to (002) plane of X1 is 60.22% of that of the bulk, which confirms the exfoliation of the bulk into nanosheets. Similarly, the intensity of X2 is only 39.73% of X1, which implies exfoliation of X2 owing to laser irradiation [51,53,57]. A clear bump between diffraction angles of 20° and 30° can be observed for X2 (**Fig. 2.8(e**)), which was not present in the case of the bulk and untreated WS_2 nanosheets. This is attributed to the oxidation of the nanosheet specimen because the signature diffraction peaks of tungsten oxides lie within this range [67]. Next, TEM micrographs of laser-treated and untreated nanosheets were analyzed. In **Fig. 2.9(a)**, **(b)** and **(c)**, HRTEM micrograph of the untreated WS_2 nanosheets are shown. The image in **Fig. 2.9(d)** shows the Inverse Fast Fourier Transformation (IFFT), as shown in **Fig. 2.9(c)**. In the inset of **Fig. 2.9(d)**, the selected area electron diffraction (SAED) spectra of the image are provided. The average fringe width of the image was found to be ~ 0.27 nm,

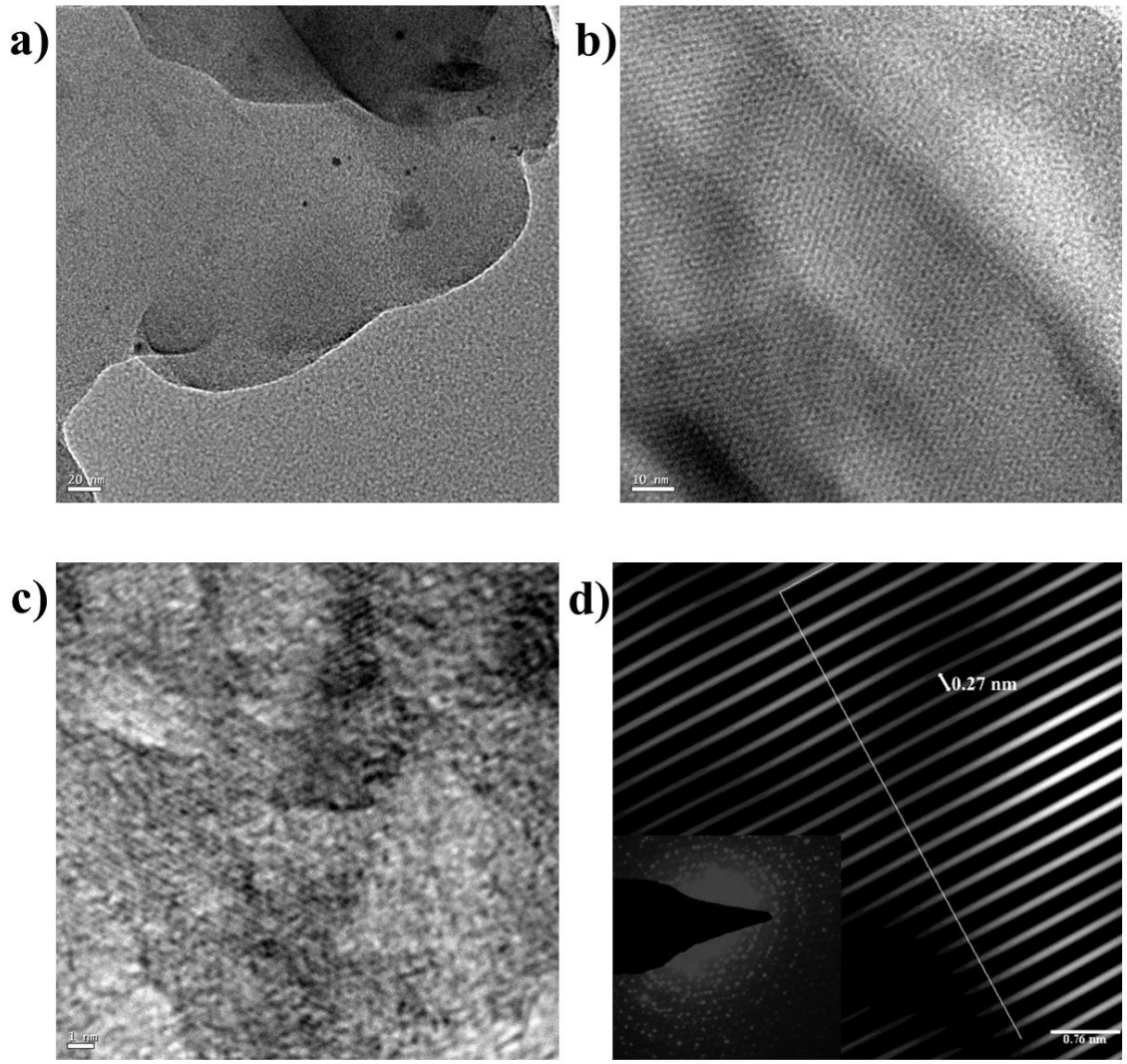

Fig.2.9. HR-TEM images of exfoliated WS_2 nanosheets with scale bar **(a)** 20 nm **(b)** 10 nm and **(c)** 1 nm respectively **(d)** IFFT of **Fig. 2.9(c)**. SAED image of exfoliated WS_2 nanosheets in the inset.

which is the characteristic *d*-spacing of the (100) plane of *2H*-WS_2 [70]. **A4**[¥] shows the plot details of **Fig. 2.9(d)**. **Fig. 2.10(a), (b),** and **(c)** show TEM micrographs of the treated nanosheets. Inorganic Fullerene (IF) like nanostructures is clearly observed in the micrographs. The shape of the obtained nanostructures is approximately spherical and closed in nature. The nanostructures were not fully detached from each-other and were not perfectly crystalline. Some structures were ~50 nm in diameter, while others were ~30 nm in diameter. Because of the numerous edge dislocations, the nanostructures were curved; however, they were not fully closed. The core of the nanostructures did not appear to be hollow. Most of the layers appeared to have started the crystallization process, but the short irradiation time (maximum 40 s) did not allow them to complete this process. The top layers are interspersed with the WS_2 layers of the adjacent nanostructures, making this

[¥]**Appendix**

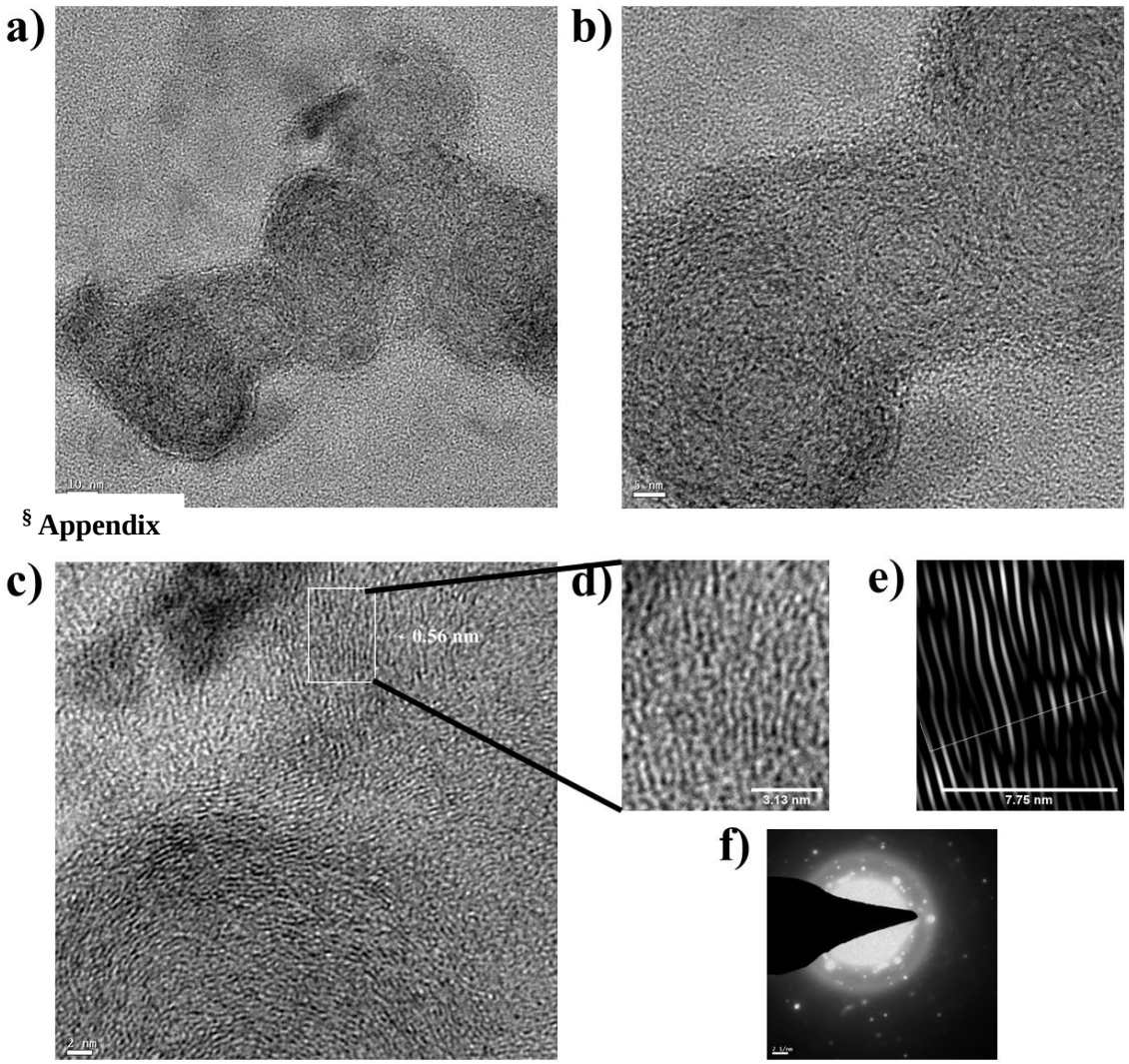

Fig.2.10. HRTEM images of laser treated WS_2 nanosheets with scale bar **(a)** 10 nm **(b)** 5 nm and **(c)** 2 nm respectively **(d)** Zoomed in image (top centre portion) of **Fig 2.10(c)**, **(e)** IFFT of **Fig. 2.10(d)**, **(f)** SAED image of exfoliated WS_2 nanosheets.

whole agglomerate inseparable. **Fig. 2.10(d)** shows an enlarged image of the top-middle portion of **Fig. 2.10(c)**. **Fig. 2.10(e)** is the IFFT of **Fig. 2.10(c)**. As shown in **Fig. 2.10(e)**, the *d*-spacing was calculated to be 0.55 nm, which is less than the standard interlayer distance of WS_2 i.e., 0.61 nm. **A5**§ shows the plot details of **Fig. 2.10(e**). **Fig. 2.10(f)** shows SAED of the laser treated WS_2 nanosheets. Laser irradiation is an intense, local thermal agitation process, known as photothermal process. According to Deepak *et al.*, photothermal processes for synthesis of IF are not fully understood till date and the products of these processes are not controllable [71]. The effects of photothermal process can be related to the thermal treatment processes. Accordingly, it effects the vibrational modes of the system. At constant pressure, the frequencies of the Raman active modes

explicitly depend on temperature (T) (at constant volume) as well as on varying volume (V) with temperature. The relation can be expressed as follows [72] -

$$\left(\frac{\partial \ln \omega}{\partial T}\right)_P = \left(\frac{\partial \ln V}{\partial T}\right)_P \left(\frac{\partial \ln \omega}{\partial \ln V}\right)_T + \left(\frac{\partial \ln \omega}{\partial T}\right)_V$$

$$= -\frac{\gamma}{k}\left(\frac{\partial \ln \omega}{\partial P}\right)_T + \left(\frac{\partial \ln \omega}{\partial T}\right)_V$$

where ω is the frequency of vibration of the Raman modes at temperature T. γ and k are the thermal coefficient and isothermal volume compressibility, respectively. The Raman modes E^1_{2g} (associated with in-plane vibration) and A_{1g} (out-of-plane vibration) of single-layer WS_2 change (decrease) linearly with an increase in the temperature from 77 K to 623 K [73]. Similar results were obtained for few-layer WS_2 and MoS_2 [22, 74]. Again, redshifts in the E^1_{2g} and A_{1g} modes with increasing laser power have been reported for MoS_2 and WSe_2 [58,59]. Therefore, redshift of E^1_{2g} and A_{1g} in the present case corroborate earlier findings. Under ambient conditions, tungsten disulfides are more unstable than tungsten oxides [75]. However, theoretical studies state that perfect 2D semiconducting transition metal di-chalcogenide crystals are indifferent to oxidation. Defect induction in the material is essential for its oxidation. It has been theoretically investigated that, compared to the pristine surface, oxygen adsorption and subsequent dissociation kinetic barriers are always less [76] on defective surfaces. To pave the way for oxygen diffusion in the material system, the system must overcome the activation energy barrier associated with the sulfur (S) defect induction in the system [77]. The threshold energy required to break this barrier depends on the temperature, time (energy and power), thickness,

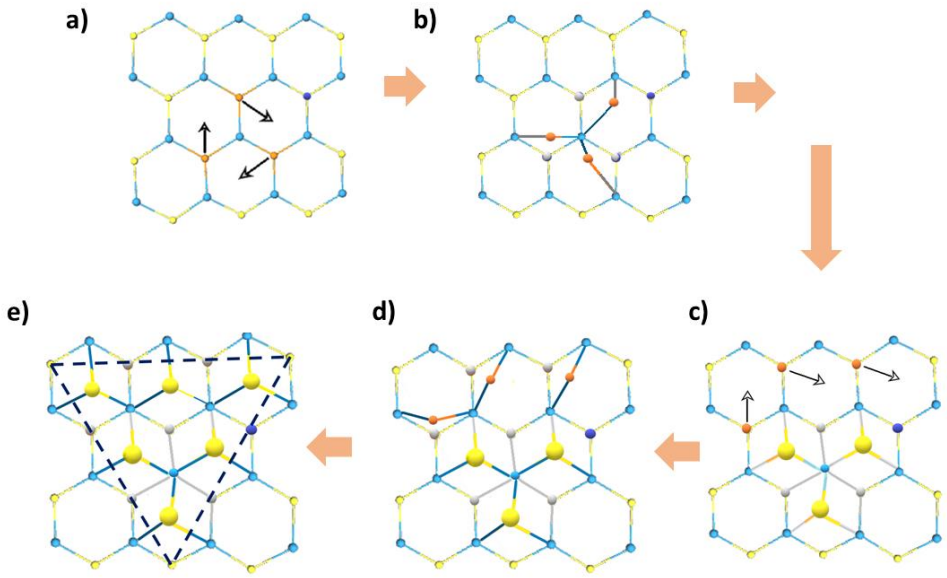

Fig. 2.11. Steps for *1T* phase nucleation on the basal plane of WS_2 with one S vacancy. Light blue balls represent Tungsten (W), yellow balls represent sulfur (S), dark blue balls represent S vacancy. Large yellow balls and grey S atoms form the nucleated *1T* phase of WS_2 (adapted from [79]).

substrate, availability of oxygen, etc. [53,78]. In the present study, the minimum available energy that had to be applied for oxidation was 50 mJ (5 mW, 10 s) and the maximum energy applied to the system was 200 mJ (5 mW, 40 s). These S defects on the WS_2 surface acted as reactive centers for oxygen dissociation and adsorption [78]. With an increase in the laser fluence, local sulfur defects were created in the WS_2 nanosheets. As the irradiation was performed in the presence of air, at a certain applied energy, the oxygen molecules attained sufficient energy to diffuse into the WS_2 nanosheet system and form a tungsten oxide-dominated WS_2 nanosystem. Thus, oxidation occurred in the present system. Cho *et al.* [51] performed a laser-induced phase transition in $MoTe_2$ and concluded that telluride (Te) monovacancy is the origin of the stable phase transition from *2H* to *1T'* of the $MoTe_2$ system. As WS_2 possesses the same starting crystal structure as $MoTe_2$, that is, $2H_c$ (hexagonal polymorph characterized by CaC AcA stacking) under normal conditions, a similar attribution can be prescribed to the present WS_2 system subjected to laser irradiation. Jin *et al.* reported several plausible atomic mechanisms of the phase transition in two-dimensional transition metal dichalcogenides, especially for the nucleation and propagation of the *1T* phase (incorporating both *1T* and *1T'*) from the $2H_c$ phase. According to them, when the basal plane of the crystal has only one S vacancy, 1T phase nucleation occurs by the collective rotational movement of three S atoms. In the propagation step, the rotational/translational movement of three S atoms takes place,

which gives rise to a triangular shape of the *1T* phase [79]. Therefore, considering both the pre-established experimental and theoretical explanations, it can be asserted that in the present system, mono S vacancies were produced due to laser irradiation. Then, the *1T* phase nucleation started with the collective rotational movement of the three S atoms. In the propagation step, a collective rotational/translational movement of three neighboring atoms occured, forming the ultimate shape of the *1T* phase. **Fig. 2.11** shows the nucleation steps of the *1T* phase. Light blue balls represent Tungsten (W), yellow balls represent S, dark blue balls represent S vacancy. Large yellow balls and gray S atoms form the nucleated *1T* phase of WS_2. **Fig. 2.11(a)** and **(b)** show the rotation of three S atoms in the basal plane of WS_2, **(c)** shows the rotational and translational movements of S atoms, and **(d)** and **(e)** show the formation of the *1T* phase and its growth. Thus, the induced defects initiated the conversion process of WS_2 from the *2H* to *1T* phase. The photoinduced effects were enhanced with subsequent irradiation doses as further increase in the laser power led to bending of the system, thus initiating the formation of IFs. However, as the process of photoirradiation was short, therefore, the obtained IFs are not perfectly crystalline in nature.

2.4 Conclusion

This chapter elucidates the solvo-sonication method for exfoliation of TMDC materials. It has also explained the data obtained from different characterizations. Then it covers the laser-induced phenomena in the material system. At first, exfoliation of bulk WS_2 flakes was carried out using NMP (organic solvent) to synthesize multilayered WS_2 nanosheets with hexagonal symmetry. Then crystallographic, vibrational, morphological and optical characterizations of the as-synthesized nanosheets were performed. Finally, laser-irradiation was performed on WS_2 nanosheets with 514 nm laser line. It was observed that laser-irradiation successfully initiate local phase transition in WS_2 by employing a minimum of 50 mJ of laser (λ_{exc} = 514 nm) irradiation. This process was also associated with simultaneous local oxidation and subsequent formation of inorganic fullerenes (IF). The obtained IFs were approximately spherical in shape and of 30-50 nm in diameter. They were not perfectly crystalline and not fully closed. The mechanisms of formation of IFs due to photoexcitation are not fully understood. However, the oxidation and phase transition in the WS_2 system can be explained by generation of S monovacancy due to laser irradiation in the system. Similarly, *1T* phase nucleation and propagation can be

explained by collective rotational and rotational/translational movement of three neighboring S atoms respectively.

References

[1] Hintze. *Handbuch der Mineralogie.* Viet and Co., Leipzig,1st edition, 410. 1904.

[2] Dickinson, R.G. and Pauling, L. The crystal structure of molybdenite. *Journal of the American Chemical Society*, 45(6): 1466-1471, 1923.

[3] Frindt, R.F. and Yoffe, A.D. Physical properties of layer structures: optical properties and photoconductivity of thin crystals of molybdenum disulphide. In *Proceedings of the Royal Society of London. Series A. Mathematical and Physical Sciences*, volume 273(1352), 69-83, 1963. Royal Society, London.

[4] Frindt, R.F. Single crystals of MoS_2 several molecular layers thick. *Journal of Applied Physics*, 37(4): 1928-1929, 1966.

[5] Joensen, P., Frindt, R.F. and Morrison, S.R. Single-layer MoS2. *Materials Research Bulletin*, 21(4): 457-461, 1986.

[6] Miremadi, B.K. and Morrison, S.R. The intercalation and exfoliation of tungsten disulfide. *Journal of Applied Physics*, 63(10): 4970-4974, 1988.

[7] Coleman, J.N., Lotya, M., O'Neill, A., Bergin, S.D., King, P.J., Khan, U., Young, K., Gaucher, A., De, S., Smith, R.J. and Shvets, I.V. Two-dimensional nanosheets produced by liquid exfoliation of layered materials. *Science*, 331(6017): 568-571, 2011.

[8] Tenne, R., Margulis, L., Genut, M.E. and Hodes, G. Polyhedral and cylindrical structures of tungsten disulphide. *Nature*, 360(6403): 444-446, 1992.

[9] Margulis, L., Salitra, G., Tenne, R. and Talianker, M. Nested fullerene-like structures. *Nature*, 365(6442): 113-114, 1993.

[10] Hershfinkel, M., Gheber, L.A., Volterra, V., Hutchison, J.L., Margulis, L. and Tenne, R. Nested polyhedra of MX_2 (M= W, Mo; X= S, Se) probed by high-resolution electron

microscopy and scanning tunneling microscopy. *Journal of the American Chemical Society*, 116(5): 1914-1917, 1994.

[11] Yang, H., Liu, S., Li, J., Li, M., Peng, G. and Zou, G. Synthesis of inorganic fullerene-like WS_2 nanoparticles and their lubricating performance. *Nanotechnology*, 17(5): 1512, 2006.

[12] Hazarika, S.J. and Mohanta, D. Inorganic fullerene-type WS_2 nanoparticles: processing, characterization and its photocatalytic performance on malachite green. *Applied Physics A*, 123(5): 1-10, 2017.

[13] Parilla, P.A., Dillon, A.C., Parkinson, B.A., Jones, K.M., Alleman, J., Riker, G., Ginley, D.S. and Heben, M.J. Formation of nanooctahedra in molybdenum disulfide and molybdenum diselenide using pulsed laser vaporization. *The Journal of PhysicalChemistry B*, 108(20): 6197-6207, 2004.

[14] Sen, R., Govindaraj, A., Suenaga, K., Suzuki, S., Kataura, H., Iijima, S. and Achiba, Y. Encapsulated and hollow closed-cage structures of WS_2 and MoS_2 prepared by laser ablation at 450–1050 C. *Chemical Physics Letters*, 340(3-4): 242-248, 2001.

[15] Savva, K., Visic, B., Popovitz-Biro, R., Stratakis, E. and Tenne, R. Short pulse laser synthesis of transition-metal dichalcogenide nanostructures under ambient conditions. *ACS Omega*, 2(6): 2649-2656, 2017.

[16] Balati, A., Bazilio, A., Shahriar, A., Nash, K. and Shipley, H.J. Simultaneous formation of ultra-thin MoSe2 nanosheets, inorganic fullerene-like $MoSe_2$ and MoO_3 quantum dots using fast and ecofriendly pulsed laser ablation in liquid followed by microwave treatment. *Materials Science in Semiconductor Processing*, 99: 68–77, 2019.

[17] Panchu, S.J., Dhani, S., Chuturgoon, A. and Moodley, M.K. Laser assisted synthesis of inorganic fullerene like MoS_2-Au nanohybrid and their cytotoxicity against human monocytic (THP-1) cells. *Journal of Photochemistry and Photobiology B: Biology*, 187: 10-17, 2018.

[18] Kolobov, A.V. and Tominaga, J. *Two-dimensional transition-metal dichalcogenides*. Springer International Publishing, Switzerland, 239,1st edition, 2016.

[19] Niu, Y., Gonzalez-Abad, S., Frisenda, R., Marauhn, P., Drüppel, M., Gant, P., Schmidt, R., Taghavi, N.S., Barcons, D., Molina-Mendoza, A.J. and De Vasconcellos, S.M. Thickness-dependent differential reflectance spectra of monolayer and few-layer MoS_2, $MoSe_2$, WS_2 and WSe_2. *Nanomaterials*, 8(9): 725, 2018.

[20] Fang, L., Liu, D.M., Guo, Y., Liao, Z.M., Luo, J.B. and Wen, S.Z. Thickness dependent friction on few-layer MoS_2, WS_2, and WSe_2. *Nanotechnology*, 28(24): 245703, 2017.

[21] Loh, T.A., Chua, D.H. and Wee, A.T. One-step synthesis of few-layer WS_2 by pulsed laser deposition. *Scientific Reports*, 5(1): 1-9, 2015.

[22] Thripuranthaka, M., Kashid, R.V., Sekhar Rout, C. and Late, D.J. Temperature dependent Raman spectroscopy of chemically derived few layer MoS_2 and WS_2 nanosheets. *Applied Physics Letters*, 104(8): 081911, 2014.

[23] Elías, A.L., Perea-López, N., Castro-Beltrán, A., Berkdemir, A., Lv, R., Feng, S., Long, A.D., Hayashi, T., Kim, Y.A., Endo, M. and Gutiérrez, H.R. Controlled synthesis and transfer of large-area WS_2 sheets: from single layer to few layers. *ACS Nano*, 7(6): 5235-5242, 2013.

[24] Perea-López, N., Elías, A.L., Berkdemir, A., Castro-Beltran, A., Gutiérrez, H.R., Feng, S., Lv, R., Hayashi, T., López-Urías, F., Ghosh, S. and Muchharla, B. Photosensor device based on few-layered WS_2 films. *Advanced Functional Materials*, 23(44): 5511-5517, 2013.

[25] Zhang, S., Dong, N., McEvoy, N., O'Brien, M., Winters, S., Berner, N.C., Yim, C., Li, Y., Zhang, X., Chen, Z. and Zhang, L. Direct observation of degenerate two-photon absorption and its saturation in WS_2 and MoS_2 monolayer and few-layer films. *ACS Nano*, 9(7): 7142-7150, 2015.

[26] Zhao, W., Ribeiro, R.M., Toh, M., Carvalho, A., Kloc, C., Castro Neto, A.H. and Eda, G. Origin of indirect optical transitions in few-layer MoS_2, WS_2, and WSe_2. *Nano Letters*, 13(11): 5627-5634, 2013.

[27] Berkdemir, A., Gutiérrez, H.R., Botello-Méndez, A.R., Perea-López, N., Elías, A.L., Chia, C.I., Wang, B., Crespi, V.H., López-Urías, F., Charlier, J.C. and Terrones, H. Identification of individual and few layers of WS_2 using Raman Spectroscopy. *Scientific Reports*, 3(1): 1-8, 2013.

[28] Bhatt, S.V., Deshpande, M.P., Sathe, V., Rao, R. and Chaki, S.H. Raman spectroscopic investigations on transition-metal dichalcogenides MX_2 (M= Mo, W; X= S, Se) at high pressures and low temperature. *Journal of Raman Spectroscopy*, 45(10): 971-979, 2014.

[29] Lee, C., Yan, H., Brus, L.E., Heinz, T.F., Hone, J. and Ryu, S. Anomalous lattice vibrations of single-and few-layer MoS_2. *ACS Nano*, 4(5): 2695-2700, 2010.

[30] Ghorai, A., Midya, A., Maiti, R. and Ray, S.K. Exfoliation of WS_2 in the semiconducting phase using a group of lithium halides: A new method of Li intercalation. *Dalton Transactions*, 45(38): 14979-14987, 2016.

[31] Mak, K.F., Lee, C., Hone, J., Shan, J. and Heinz, T.F. Atomically thin MoS_2: a new direct-gap semiconductor. *Physical Review Letters*, 105(13): 136805, 2010.

[32] Eda, G., Yamaguchi, H., Voiry, D., Fujita, T., Chen, M. and Chhowalla, M. Photoluminescence from chemically exfoliated MoS_2. *Nano Letters*, 11(12):5111-5116, 2011.

[33] Beal, A.R., Knights, J.C. and Liang, W.Y. Transmission spectra of some transition metal dichalcogenides. II. Group VIA: trigonal prismatic coordination. *Journal of Physics C: Solid State Physics*, 5(24): 3540, 1972.

[34] Bromley, R.A., Murray, R.B. and Yoffe, A.D. The band structures of some transition metal dichalcogenides. III. Group VIA: trigonal prism materials. *Journal of Physics C: Solid State Physics*, 5(7): 759, 1972.

[35] Mattheiss, L.F.Band structures of transition-metal-dichalcogenide layer compounds. *Physical Review B*, 8(8): 3719–3740,1973.

[36] Wilson, J.A., Di Salvo, F.J. and Mahajan, S. Charge-density waves and superlattices in the metallic layered transition metal dichalcogenides. *Advances in Physics*, 24(2):117-201, 1975.

[37] Suzuki, R., Sakano, M., Zhang, Y.J., Akashi, R., Morikawa, D., Harasawa, A., Yaji, K., Kuroda, K., Miyamoto, K., Okuda, T. and Ishizaka, K. Valley-dependent spin polarization in bulk MoS_2 with broken inversion symmetry. *Nature Nanotechnology*, 9(8): 611-617, 2014.

[38] H. Luo, W. Xie, J. Tao, H. Inoue, A. Gyenis, J.W. Krizan, A. Yazdani, Y. Zhu, R. J. Cava, Polytypism, polymorphism, and superconductivity. In $TaSe_{2-x}Te_x$. *Proceedings of the National Academy of Sciences*, volume 112(11), E1174–E1180, 2015. PNAS, USA.

[39] Yoshida, M., Ye, J., Zhang, Y., Imai, Y., Kimura, S., Fujiwara, A., Nishizaki, T., Kobayashi, N., Nakano, M. and Iwasa, Y. Extended polymorphism of two-dimensional material. *Nano Letters*, 17(9): 5567-5571, 2017.

[40] Voiry, D., Yamaguchi, H., Li, J., Silva, R., Alves, D.C., Fujita, T., Chen, M., Asefa, T., Shenoy, V.B., Eda, G. and Chhowalla, M. Enhanced catalytic activity in strained chemically exfoliated WS_2 nanosheets for hydrogen evolution. *Nature Materials*, 12(9): 850-855, 2013.

[41] Leong, S.X., Mayorga-Martinez, C.C., Chia, X., Luxa, J., Sofer, Z. and Pumera, M. 2H→ 1T phase change in direct synthesis of WS_2 nanosheets via solution-based electrochemical exfoliation and their catalytic properties. *ACS Applied Materials & Interfaces*, 9(31): 26350-26356, 2017.

[42] Friedman, A.L., Hanbicki, A.T., Perkins, F.K., Jernigan, G.G., Culbertson, J.C. and Campbell, P.M. Evidence for chemical vapor induced 2H to 1T phase transition in MoX_2 (X= Se, S) transition metal dichalcogenide films. *Scientific Reports*, 7(1): 1-9, 2017.

[43] Chen, X., Chen, Z. and Li, J. Critical electronic structures controlling phase transitions induced by lithium ion intercalation in molybdenum disulphide. *Chinese Science Bulletin*, 58(14): 1632-1641, 2013.

[44] Wang, L., Xu, Z., Wang, W. and Bai, X. Atomic mechanism of dynamic electrochemical lithiation processes of MoS_2 nanosheets. *Journal of the American Chemical Society*, 136(18): 6693-6697, 2014.

[45] Thomas, A., Vikram, K., Muthu, D.V.S. and Sood, A.K. Structural phase transition from 1H to 1T′ at low pressure in supported monolayer WS_2: Raman study. *Solid State Communications*, 336: 114412, 2021.

[46] Kosmala, T., Palczynski, P., Amati, M., Gregoratti, L., Sezen, H., Mattevi, C., Agnoli, S. and Granozzi, G. Strain induced phase transition of WS_2 by local dewetting of Au/Mica film upon annealing. *Surfaces*, 4(1): 1-8, 2020.

[47] Thakur, D., Kumar, P. and Balakrishnan, V. Phase selective CVD growth and photoinduced 1T→ 1H phase transition in a WS_2 monolayer. *Journal of Materials Chemistry C*, 8(30): 10438-10447, 2020.

[48] Cheng, Y., Nie, A., Zhang, Q., Gan, L.Y., Shahbazian-Yassar, R. and Schwingenschlogl, U. Origin of the phase transition in lithiated molybdenum disulfide. *ACS Nano*, 8(11): 11447-11453, 2014.

[49] Leng, K., Chen, Z., Zhao, X., Tang, W., Tian, B., Nai, C.T., Zhou, W. and Loh, K.P. Phase restructuring in transition metal dichalcogenides for highly stable energy storage. *ACS Nano*, 10(10): 9208-9215, 2016.

[50] Lin, Y.C., Dumcenco, D.O., Huang, Y.S. and Suenaga, K. Atomic mechanism of the semiconducting-to-metallic phase transition in single-layered MoS_2. *Nature Nanotechnology*, 9(5): 391-396, 2014.

[51] Cho, S., Kim, S., Kim, J.H., Zhao, J., Seok, J., Keum, D.H., Baik, J., Choe, D.H., Chang, K.J., Suenaga, K. and Kim, S.W Phase patterning for ohmic homojunction contact in $MoTe_2$. *Science*, 349(6248): 625-628, 2015.

[52] Fan, X., Xu, P., Zhou, D., Sun, Y., Li, Y.C., Nguyen, M.A.T., Terrones, M. and Mallouk, T.E. Fast and efficient preparation of exfoliated 2H MoS_2 nanosheets by sonication-assisted lithium intercalation and infrared laser-induced 1T to 2H phase reversion. *Nano Letters*, 15(9): 5956-5960, 2015.

[53] Chen, Z., Nan, H., Liu, Z., Wang, X., Gu, X. and Xiao, S. Effect of thermal conductivity of substrate on laser-induced phase transition of $MoTe_2$. *Journal of Raman Spectroscopy*, 50(5): 755-761, 2019.

[54] Wang, M., Li, D., Liu, K., Guo, Q., Wang, S. and Li, X. Nonlinear optical imaging, precise layer thinning, and phase engineering in $MoTe_2$ with femtosecond laser. *ACS Nano*, 14(9): 11169-11177, 2020.

[55] Li, H., Lu, G., Wang, Y., Yin, Z., Cong, C., He, Q., Wang, L., Ding, F., Yu, T. and Zhang, H. Mechanical exfoliation and characterization of single-and few-layer nanosheets of WSe_2, TaS_2, and $TaSe_2$. *Small*, 9(11): 1974-1981, 2013.

[56] Tan, C., Liu, Y., Chou, H., Kim, J.S., Wu, D., Akinwande, D. and Lai, K. Laser-assisted oxidation of multi-layer tungsten diselenide nanosheets. *Applied Physics Letters*, 108(8): 083112, 2016.

[57] Castellanos-Gomez, A., Barkelid, M., Goossens, A.M., Calado, V.E., van der Zant, H.S. and Steele, G.A. Laser-thinning of MoS_2: on demand generation of a single-layer semiconductor. *Nano Letters*, 12(6): 3187-3192, 2012.

[58] Sahoo, S., Gaur, A.P., Ahmadi, M., Guinel, M.J.F. and Katiyar, R.S. Temperature-dependent Raman studies and thermal conductivity of few-layer MoS_2. *The Journal of Physical Chemistry C*, 117(17): 9042-9047, 2013.

[59] Bandyopadhyay, A.S., Biswas, C. and Kaul, A.B. Light–matter interactions in two-dimensional layered WSe_2 for gauging evolution of phonon dynamics. *Beilstein journal of nanotechnology*, 11(1): 782-797, 2020.

[60] Zhu, J., Huang, X. and Song, W. Physical and Chemical Sensors on the Basis of Laser-Induced Graphene: Mechanisms, Applications, and Perspectives. *ACS Nano*, 15(12): 18708-18741, 2021.

[61] Eva, A.A. and Conte, S. Exciton and charge carrier dynamics in few-layer WS_2. *Nanoscale*, 8(10): 5428-5434, 2016.

[62] Atkin, P., Daeneke, T., Wang, Y., Carey, B.J., Berean, K.J., Clark, R.M., Ou, J.Z., Trinchi, A., Cole, I.S. and Kalantar-Zadeh, K. 2D WS_2/carbon dot hybrids with enhanced photocatalytic activity. *Journal of Materials Chemistry A*, 4(35): 13563-13571, 2016.

[63] Zhao, W., Ghorannevis, Z., Chu, L., Toh, M., Kloc, C., Tan, P.H. and Eda, G. Evolution of electronic structure in atomically thin sheets of WS_2 and WSe_2. *ACS Nano*, 7(1): 791-797, 2013.

[64] Ramasubramaniam, A. Large excitonic effects in monolayers of molybdenum and tungsten dichalcogenides. *Physical Review B*, 86(11): 115409, 2012.

[65] Salje, E. Lattice dynamics of WO_3. *Acta Crystallographica Section A: Crystal Physics, Diffraction, Theoretical and General Crystallography*, 31(3): 360-363, 1975.

[66] Daniel, M.F., Desbat, B., Lassegues, J.C., Gerand, B. and Figlarz, M. Infrared and Raman study of WO_3 tungsten trioxides and WO_3, xH_2O tungsten trioxide tydrates. *Journal of Solid State Chemistry*, 67(2): 235-247, 1987.

[67] Santato, C., Odziemkowski, M., Ulmann, M. and Augustynski, J. Crystallographically oriented mesoporous WO_3 films: synthesis, characterization, and applications. *Journal of the American Chemical Society*, 123(43): 10639-10649, 2001.

[68] Liu, Z., Li, P., Dong, Y., Wan, Q., Zhai, F., Volinsky, A.A. and Qu, X. Facile preparation of hexagonal $WO_3 \cdot 0.33\ H_2O$/C nanostructures and its electrochemical properties for lithium-ion batteries. *Applied Surface Science*, 394: 70-77, 2017.

[69] Liu, Z., Li, N., Su, C., Zhao, H., Xu, L., Yin, Z., Li, J. and Du, Y. Colloidal synthesis of 1T'phase dominated WS_2 towards endurable electrocatalysis. *Nano Energy*, 50: 176-181, 2018.

[70] Rout, C.S., Joshi, P.D., Kashid, R.V., Joag, D.S., More, M.A., Simbeck, A.J., Washington, M., Nayak, S.K. and Late, D.J. Superior field emission properties of layered WS_2-RGO nanocomposites. *Scientific Reports*, 3(1): 1-8, 2013.

[71] Deepak, F. and Tenne, R. Gas-phase synthesis of inorganic fullerene-like structures and inorganic nanotubes. *Open Chemistry*, 6(3): 373-389, 2008.

[72] Peercy, P.S. and Morosin, B. Pressure and temperature dependences of the Raman-active phonons in SnO_2. *Physical Review B*, 7(6): 2779, 1973.

[73] Thripuranthaka, M., Late, D.J. Temperature dependent phonon shifts in single-layer WS_2. *ACS Applied Materials & Interfaces*, 6(2): 1158-1163, 2014.

[74] Sinha, S., Sathe, V. and Arora, S.K. Temperature dependent Raman investigations of few-layered WS_2 nanosheets. *Solid State Communications*, 298: 113626, 2019.

[75] Gale, W.F. and Totemeier, T.C. Smithells Metals Reference Book. Elsevier Butterworth- Heinemann, Oxford, 8th edition, 2004.

[76] Kc, S., Longo, R.C., Wallace, R.M. and Cho, K. Surface oxidation energetics and kinetics on MoS_2 monolayer. *Journal of Applied Physics*, 117(13): 135301, 2015.

[77] Adigilli, H.K., Padya, B., Venkatesh, L., Chakravadhanula, V.S.K., Pandey, A.K. and Joardar, J. Oxidation of 2D-WS_2 nanosheets for generation of 2D-WS_2/WO_3 heterostructure and 2D and nanospherical WO_3. *Physical Chemistry Chemical Physics*, 21(45): 25139-25147, 2019.

[78] Liu, H., Han, N. and Zhao, J. Atomistic insight into the oxidation of monolayer transition metal dichalcogenides: from structures to electronic properties. *Rsc Advances*, 5(23): 17572-17581, 2015.

[79] Jin, Q., Liu, N., Chen, B. and Mei, D. Mechanisms of semiconducting 2H to metallic 1T phase transition in two-dimensional MoS_2 nanosheets. *The Journal of Physical Chemistry C*, 122(49): 28215-28224, 2018.